Effects of embedded walls on tunnelling-induced sandy ground displacements: a numerical investigation

Jingmin Xu[a,b], Luorui Zheng[a], Geyang Song[c]*, Dingwen Zhang[a], Brian Sheil[b], Alec M Marshall[d]

[a] School of Transportation, Southeast University, Nanjing, 211189, China

[b] Department of Engineering, University of Cambridge, Cambridge, CB2 1TN, UK

[c] CTO JS2 Innovation Ltd., London W1W 5PF, UK; formerly, Department of Engineering Science, University of Oxford, Parks Road, Oxford, OX1 3PJ, UK

[d] Department of Civil Engineering, University of Nottingham, Nottingham, NG7 2RD, UK

*Corresponding author Email: geyang.song@js2innovation.com

Abstract

Urban tunnelling projects pose significant risks to the integrity of nearby structures due to ground movements induced by the excavation process. Embedded walls are commonly employed as a protective measure to mitigate these adverse effects. This paper presents a comprehensive numerical investigation into the effects of embedded walls on tunnelling-induced ground displacements, aiming to provide insights and recommendations for optimal embedded wall design. The study assesses the impact of varying embedded wall length and horizontal distance from the tunnel on soil settlement and horizontal displacements. Results demonstrate the complex interplay between embedded wall length, horizontal distance, and ground movement patterns, and the highly non-linear influence of key parameters on embedded wall efficiency (i.e. its ability to reduce settlements). A preliminary design chart is proposed to guide engineers in determining the appropriate horizontal location and depth of embedded walls to effectively reduce tunnelling-

induced ground displacements. The findings contribute to a better understanding of embedded wall performance in the context of tunnelling and provide valuable guidance for the practical design and implementation of protective measures in urban areas.

Keywords: Diaphragm & in situ walls; Ground movements; Numerical modelling; Soil/structure interaction; Tunnels & Tunnelling

Notation

C	cover depth	U_x	horizontal displacement
d_w	embedded wall horizontal distance to the tunnel	U_z	settlement
D_{50}	sand average diameter	$U_{z,bw}$	soil settlement behind the embedded wall
D_t	tunnel diameter	$U_{z,ref}$	greenfield settlement at embedded wall location
e_{c0}	maximum void ratio at zero pressure	$V_{l,t}$	tunnel volume loss
e_{d0}	minimum void ratio at zero pressure	x	horizontal distance
e_{i0}	critical void ratio at zero pressure	z	depth
e_{max}	maximum void ratio of sand	z_t	tunnel axis depth
e_{min}	minimum void ratio of sand	α	exponent for hypoplastic model
EI	bending stiffness of the embedded wall	β	exponent for hypoplastic model
h_s	granular hardness	φ'_c	critical state friction angle
I_d	relative density of sand	η_{bw}^{v}	settlement efficiency
K_0	coefficient of horizontal pressure	η_{bw}^{h}	horizontal efficiency
L_w	length of the embedded wall	η_{bw}^{s}	slope efficiency
M	bending moment	ρ_s	soil density
n	exponent for hypoplastic model	ρ_w	density of the embedded wall
t	embedded wall thickness		

1 Introduction

Tunnelling in urban areas inevitably leads to stress relief and movements in the surrounding ground, which in turn may have detrimental effects on nearby structures. To prevent damage to buildings from tunnelling, various protective measures have been adopted to inhibit tunnelling-induced ground movements. The parameters and specifics of the chosen countermeasure require meticulous planning and design to safeguard buildings from potential adverse effects of tunnelling whilst ensuring cost-effective tunnel construction.

Protective measures can be categorised into three groups: in-tunnel measures, ground treatment measures, and structural measures (Harris, 2001). Among these, structural measures are commonly used to mitigate tunnelling-induced ground movements and structural deformation when tunnels are excavated near buildings. This approach typically involves the construction of an intervening row of piles or an embedded wall. In practice, structural measures are popular as they provide an immediate and efficient control method. Ledesma and Alonso (2017) presented a case study in which a row of reinforced concrete piles was used to protect sensitive buildings from tunnelling-induced damage. Monitoring results indicated that soil displacements were considerably lower than the predicted values at the design stage. Similarly, Di Mariano et al. (2007) described the use of a row of bored cast-in-situ piles to safeguard several seven-storey residential buildings from tunnelling-induced displacements. The observed results revealed that the settlement curve shape was altered substantially, and the building damage was decreased from category 3 to 0 (from moderate to negligible based on Burland (2001)). Gens et al. (2005) documented the use of micropile ‘screens’ to mitigate the effects of tunnelling on a primary urban motorway. Interestingly, the final ground settlements were caused primarily by the construction of the micropiles themselves whereas tunnelling-induced settlements were minimal. Losacco and Viggiani (2019) also demonstrated the ability of an embedded barrier of bored piles to protect historic monuments from the construction of Line C of the Rome underground.

To provide guidance for practice, it is desirable to identify the optimal embedded wall geometric and material parameters to minimise tunnelling-induced ground movements. Bilotta (2008) and Bilotta and Stallebrass (2009) described a centrifuge testing and complementary numerical modelling programme exploring the influence of embedded diaphragm wall length on settlements caused by nearby tunnelling in clay; it was concluded that the embedded wall's effectiveness was highly dependent on its length. Similarly, Song and Marshall (2021) used geotechnical centrifuge test results to show that a 'deep' embedded wall significantly reduced uneven pile settlements and structural distortions, whereas a 'shallow' embedded wall offered minimal benefits. A further numerical study by Song et al. (2023) identified an optimal depth of an embedded wall for reducing piled building damage due to tunnelling. However, these studies only considered a single case where the building and embedded wall were located very close to the tunnel. Bilotta and Russo (2011) used numerical analyses to highlight the pile spacing ratio as one of the key geometric parameters for a row of piles to mitigate ground displacements in stiff clay. A recent study by Rampello et al. (2019) confirmed that the soil-structure interface roughness also plays a role: a barrier with a smoother surface tends to achieve higher efficiency. Interestingly, Rampello et al. (2019) also showed that a shorter barrier farther away from the tunnel might have a similar reduction effect on the settlement compared to a deeper barrier placed closer to the tunnel, highlighting the complex dependence of results on the horizontal proximity of the embedded wall to the tunnel. Employing a simplified elastic continuum-based two-stage model, Franza et al. (2021) compared the efficiency of "close location" and "far location" pile walls in reducing soil settlements caused by tunnelling and noted that the pile wall efficiency was underpredicted for large tunnelling-induced ground displacements (compared against field data and numerical results), which are of utmost practical interest.

To summarise, previous studies have primarily focused on the use of a line of piles or an embedded wall to mitigate tunnelling-induced damage in clay, while the scenario in sandy ground has received less attention. Furthermore, although results have demonstrated the significance of embedded wall length on its effectiveness to reduce tunnelling-induced settlement, the role of the horizontal distance of the embedded wall remains an open question. Consequently, no comprehensive guidance currently exists for optimising embedded wall parameters when employing structural measures to minimise tunnelling-induced ground movement, particularly in sand.

To address this gap, this paper presents results from a numerical study on the use of embedded walls to reduce ground displacements caused by tunnelling in sand. The advanced constitutive model known as the hypoplastic model (von Wolffersdorff, 1996) was used to simulate the soil behaviour and calibrated using data from element and centrifuge testing. A “wished-in-place” embedded wall is modelled, with outcomes providing novel insights regarding the role of the embedded wall length and its horizontal distance from the tunnel in reducing tunnelling-induced ground movements in sandy ground. First, the structural response of the embedded walls due to tunnelling is presented. This is followed by an examination of surface and subsurface soil displacements to elucidate the effects of an embedded wall on the ground movement mechanisms. Lastly, the effectiveness of the embedded walls is assessed using an efficiency parameter, followed by the suggestion of a preliminary design chart in determining the embedded wall length and location; practical implications of the results for embedded walls are also briefly discussed.

2 Finite element model

2.1 Problem definition

Figure 1 illustrates the scenario considered in this study: a tunnel with a diameter (D_t) of 7.2 m and a cover depth (C) of 12.96 m (resulting in a tunnel axis depth, z_t, of 16.56 m) is constructed in dry sand near an existing embedded wall. These dimensions are adopted to enable comparisons of the numerical results with the experimental data presented in Song and Marshall (2021); the simulations presented here are representative of the same full-scale (prototype) scenario. To examine the effects of the embedded wall's length and location in reducing tunnelling-induced ground movements, the results from 21 numerical models are considered (see Table 1): 20 tunnel-wall interaction tests (divided into three groups based on the horizontal distance of the embedded wall to the tunnel) and one greenfield test for reference. The embedded wall length (L_w) varied from 11.76 m to 23.76 m (L_w/z_t = 0.71 to 1.43), and the horizontal distance, d_w, ranged from 4.4 m to 11.6 m (d_w/D_t = 0.61 to 1.61); all embedded walls had the same thickness of 0.8 m. A singular shallow tunnelling scenario was considered because, in practice, the construction of a shallow tunnel has the greatest potential to impact neighbouring structures. A default volume loss $V_{l,t}$ =3% was adopted unless otherwise specified; this relatively high value was chosen considering that protective measures are usually adopted when a high tunnel volume loss or large ground movements are expected.

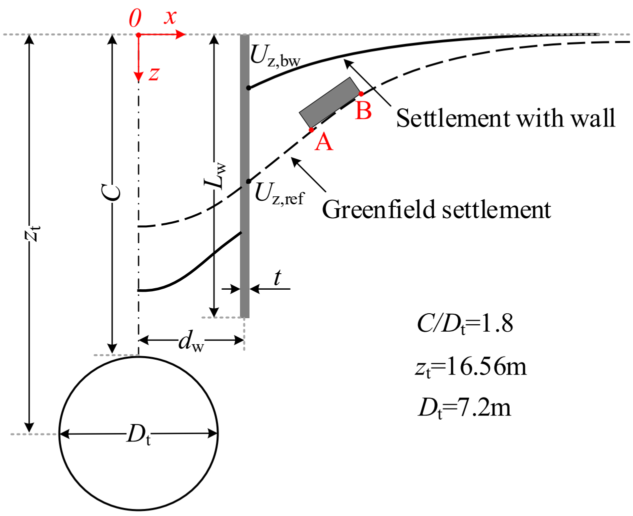

Figure 1. Illustration of the problem and parameter definition

Table 1 Overview of numerical parametric study

No	L_w: m	d_w: m	L_w/z_t	d_w/D_t	Group
1	Greenfield: reference test				-
2	11.76	4.4	0.71	0.61	
3	14.16	4.4	0.86	0.61	
4	16.56	4.4	1.00	0.61	
5	18.96	4.4	1.14	0.61	Group A
6	19.44	4.4	1.17	0.61	
7	20.16	4.4	1.22	0.61	
8	21.36	4.4	1.29	0.61	
9	23.76	4.4	1.43	0.61	
10	11.76	8.0	0.71	1.11	
11	14.16	8.0	0.86	1.11	
12	16.56	8.0	1.00	1.11	Group B
13	18.96	8.0	1.14	1.11	
14	21.36	8.0	1.29	1.11	
15	23.76	8.0	1.43	1.11	
16	11.76	11.6	0.71	1.61	
17	14.16	11.6	0.86	1.61	
18	16.56	11.6	1.00	1.61	Group C
19	18.96	11.6	1.14	1.61	
20	21.36	11.6	1.29	1.61	
21	23.76	11.6	1.43	1.61	

2.2 Element mesh and boundary conditions

The finite element (FE) analysis software ABAQUS (Hibbitt, 2002) was adopted for this study. Figure 2 shows an example FE mesh consisting of 85,507 nodes and 73,840 elements which was adopted on the basis of a mesh sensitivity study. The model's width, depth, and thickness (out-of-plane) are 7.78 D_t, 4.24 D_t and 1.67 D_t, respectively to match the prototype conditions of the Song and Marshall (2021) centrifuge tests. Eight-node brick elements (C3D8) were used to simulate the soil, while ‘incompatible’ eight-node brick elements (C3D8I - an improved version of the C3D8-element) were employed for embedded walls and the tunnel boundary. The bottom boundary of the computational domain was fixed and a vertical roller boundary was applied to all sides of the soil mesh; no constraints were applied to the soil surface.

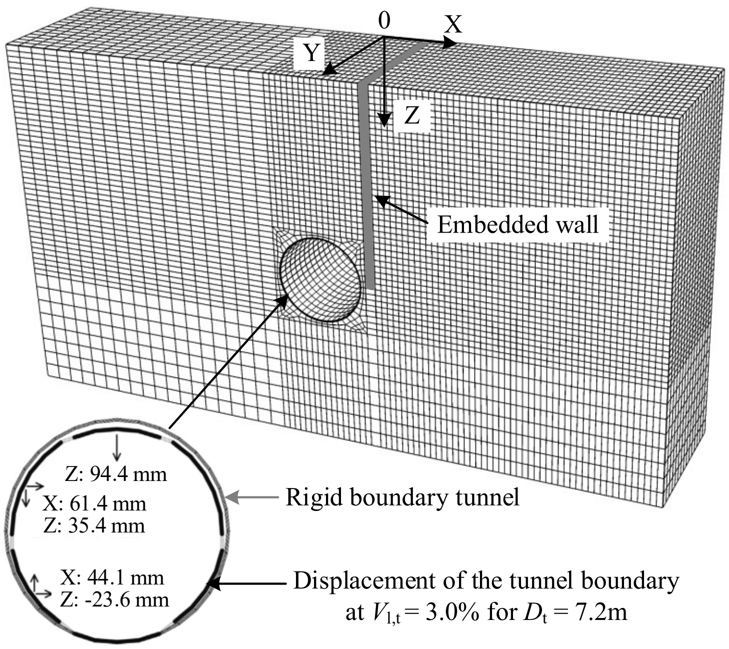

Figure 2. Typical finite element mesh showing mesh discretisation near tunnel and imposed displacement boundary conditions during the analysis (L_w/z_t =1.00, d_w/D_t =0.61; test No.4 in Table 1).

2.3 Constitutive model and model parameters

The soil constitutive model known as the hypoplastic model proposed by von Wolffersdorff (1996) was employed to simulate the behaviour of the sand. It incorporates pressure- and density-dependency of soil behaviour, and can provide reliable predictions of various sand behaviours, e.g. volumetric change due to shearing and small strain stiffness degradation (Herle and Gudehus, 1999). The hypoplastic model has been extensively used in the study of various soil-structure interaction problems and has been shown to provide predictions that are in good agreement with experimental data (Wang et al., 2022; Khalajzadeh et al., 2023; Song et al., 2023). The basic hypoplastic model has eight parameters: critical state friction angle φ'_c, granular hardness h_s, fitting parameter n, minimum/maximum/critical void ratios at zero pressure $e_{d0}/e_{i0}/e_{c0}$, and α; β, which govern the soil's stiffness. These parameters were calibrated based on data from oedometer and drained triaxial compression tests, as explained in more detail in Figures S1 and S2 in the Supplemental Materials (modified from Song and Marshall (2020a)).

To enable comparison with the centrifuge test data documented in Song and Marshall (2021), the same fine-grained silica sand ('Leighton Buzzard Fraction E') was simulated in the numerical models. This sand has an average diameter of D_{50} = 0.14 mm, and maximum (e_{max}) and minimum (e_{min}) void ratios of 1.01 and 0.61, respectively (Zhao 2008, Lanzano et al. 2016). A relative density (I_d) of 90% was considered, corresponding to a density ρ_s of 1603 kg/m^3, again to match the conditions of the centrifuge experiments. Table 2 summarises the model parameters used for the present study. The model embedded wall and tunnel are linear elastic with a Young's modulus of 70 GPa and a density ρ_w of 2700 kg/m^3 (consistent with Song and Marshall (2021)). Soil-wall and soil-tunnel interfaces were simulated using a Coulomb friction law with a friction coefficient of tan (φ'_c) = 0.62, assuming a perfectly rough soil-structure interface. An absolute elastic slip distance (1.5 mm) was used to define the tangential behaviour of the soil–wall interface, based on centrifuge pile jacking tests (Song and Marshall, 2020b). Note that, whilst the material parameters were selected to match specific experimental conditions, the outcomes from this study, in terms of the efficiency of the embedded wall, should also be applicable to a wider range of conditions.

Table 2. Hypoplastic model parameters adopted for Leighton Buzzard Fraction E sand, after Song and Marshall (2021)

Parameter	Value	Source
Critical state friction angle, φ'_c (°)	32	Heap test
Granular hardness, h_s (MPa)	1969	Oedometer test
Exponent, n	0.447	Oedometer test
Minimum void ratio at zero pressure, e_{d0}	0.624	Herle and Gudehus (1999)
Critical void ratio at zero pressure, e_{i0}	1.16	Oedometer test
Maximum void ratio at zero pressure, e_{c0}	1.392	Herle and Gudehus (1999)
Exponent, α	0.08	Triaxial test, I_d = 90%
Exponent, β	1.5	Triaxial test, I_d = 90%

2.4 Numerical modelling procedure

Tunnel construction is simulated using the displacement control method described in Song and Marshall (2020a), assuming maximum displacement at the tunnel crown and minimum deformation at the tunnel invert (see Figure 2). Firstly, a predetermined initial stress condition was imposed on the soil mesh, calculated based on the soil's self-weight and K_0=0.5. The gravity within the model was subsequently increased from 1g to 80g, followed by the application of a geostatic step. Soil elements within the tunnel and embedded walls were then eliminated, and the tunnel lining, embedded wall and soil-structure interfaces were activated in-place. Lastly, a non-uniform displacement profile was imposed on the tunnel boundary elements to emulate the effects of tunnel excavation. This displacement-control method for tunnelling has been extensively used in both centrifuge tests (Boonsiri and Takemura, 2015; Song and Marshall, 2021) and numerical modelling (Boldini et al., 2018; Fu et al., 2018).

2.5 Numerical model validation

To validate the present numerical modelling approach, greenfield tunnelling-induced surface soil displacements corresponding to a tunnel volume loss of $V_{l,t}$=3.0% obtained from both numerical (this paper) and centrifuge (Song and Marshall, 2021) models are compared in Figures 3(a) (normalised settlement U_z/D_t) and 3(b) (normalised absolute value of horizontal displacement $|U_x|/D_t$). Downward vertical displacements and horizontal displacements toward the right are defined as positive. Note that all displacements from the numerical model are those caused by tunnel volume loss (i.e., displacements due to geostatic stresses and embedded wall activation were subtracted). The numerical model predictions compare very well to the measured trends in terms of both displacement magnitude and contour distribution, which highlights the reliability of the numerical model.

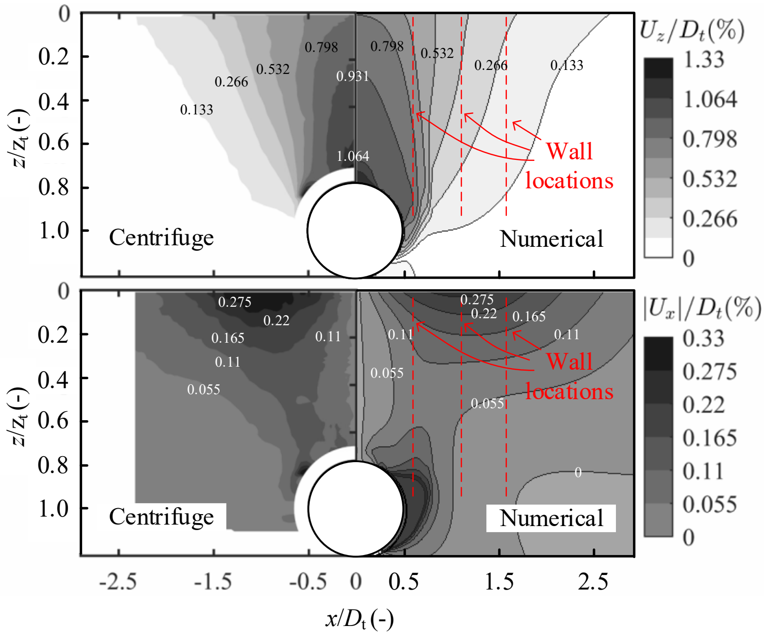

Figure 3 Comparison between FE model predictions and centrifuge test measurements of surface displacements in greenfield tests at $V_{l,t}$=3.0%: (a) normalised vertical settlements, U_z/D_t; (b) absolute value of normalised horizontal displacements, $|U_x|/D_t$ [embedded wall locations from Table 1 shown for information].

3 Results

3.1 Embedded wall response to tunnelling

Figure 4 presents depth-wise profiles of horizontal displacements of the embedded walls in the three groups, i.e., d_w/D_t =0.61, 1.11 and 1.61 (see Table 1), along with the greenfield horizontal displacements at corresponding locations. For d_w/D_t =0.61, the embedded wall rotates in a clockwise manner about a depth of approximately z/z_t = 0.5, causing positive horizontal displacements above z/z_t = 0.5 which are in the opposite direction to greenfield displacements; this response is explained in detail later. For embedded walls longer than L_w/z_t > 1.2, the base of the embedded wall is embedded in soil that experiences minimal horizontal displacements from the tunnel, with horizontal embedded wall displacement decreasing towards zero as embedded wall depth increases.

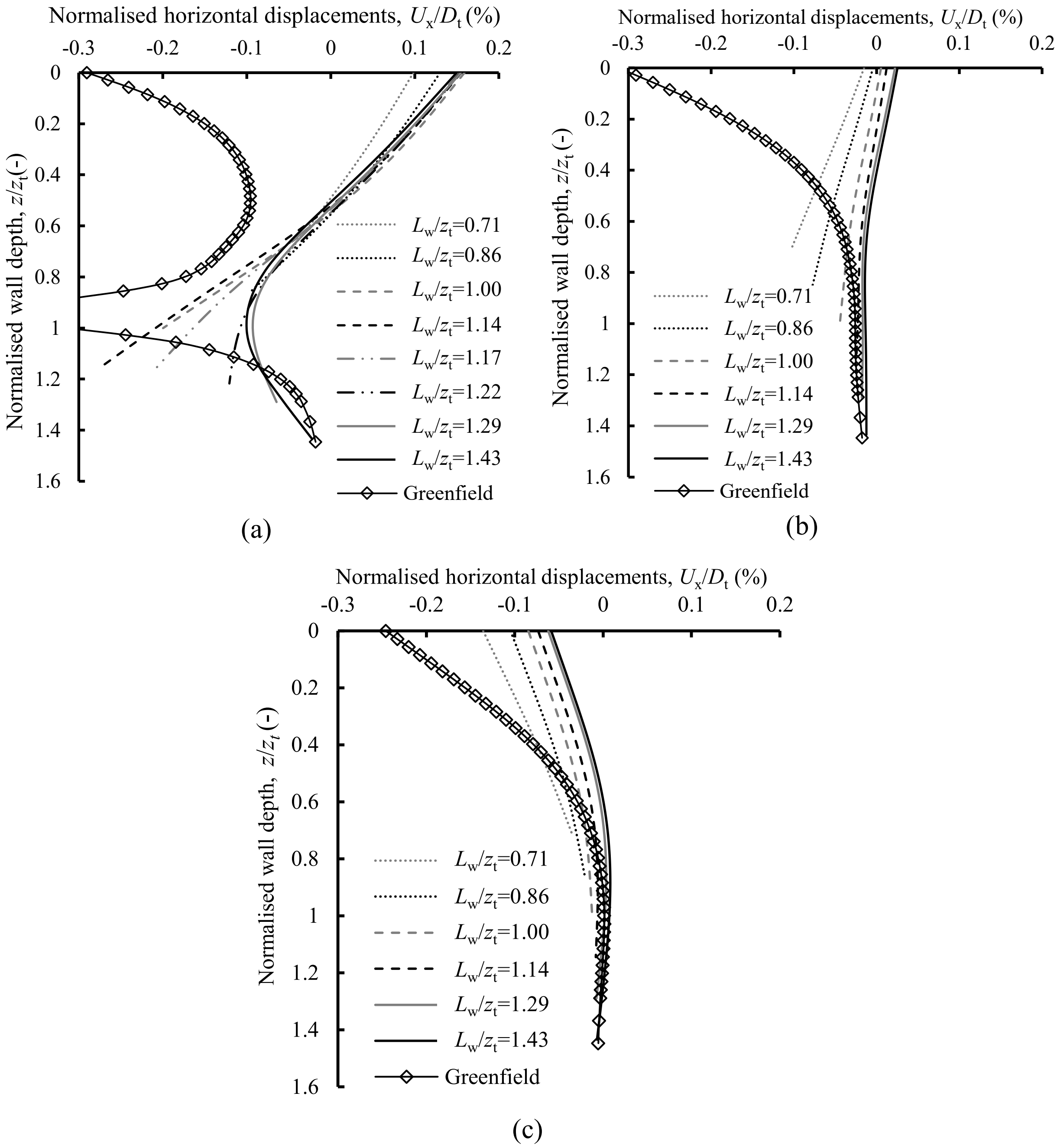

Figure 4 FE calculations of the depth-wise profiles of normalised horizontal embedded wall displacements for various embedded wall embedment depths and for embedded wall locations of (a) d_w/D_t=0.61; (b) d_w/D_t=1.11; (c) d_w/D_t=1.61; $V_{l,t}$=3.0%.

Figure 4(b) illustrates that, for the d_w/D_t =1.11 group, a rigid body motion accompanied by a clockwise rotation (greater horizontal displacement at the toe than at the top) of the embedded wall was observed for the shortest embedded wall, resulting in a negative horizontal displacement across the entire embedded wall. As the embedded wall length is increased, the toe of the embedded wall is progressively embedded into soil that experiences minimal horizontal displacements from tunnelling. The surrounding soil constrains the movement of the embedded wall toe, leading to a reduction in the embedded wall's horizontal displacement. Interestingly, the embedded wall response does not follow expectations based on the greenfield displacements at this location, which would suggest that, as the toe of the embedded wall is embedded in more stationary soil, the embedded wall should bend/rotate in an anti-clockwise manner. Instead, the embedded wall rotates/bends in a clockwise direction, similar to the results in the d_w/D_t =0.61 group; this response is examined further later in the paper with the use of contour plots of soil displacements. As expected, the embedded walls in the d_w/D_t =1.61 group showed negligible displacements at the toe of the embedded wall and negative (towards the left) horizontal displacements at the upper section of the embedded wall; the longer the embedded wall, the smaller the displacements.

In practice, the bending strength is important in the design of a embedded wall. Figure 5 illustrates the variation of normalised bending moments (Mt/EI, where M is the bending moment, t is the thickness of the embedded wall, EI is the bending stiffness of the embedded wall) with depth along the embedded walls in all numerical models. Figure 5(a) reveals that, for the embedded wall situated near the tunnel (d_w/D_t =0.61), the bending moment profiles are highly dependent on the embedded wall length. For a shorter embedded wall ($L_w/z_t < 1.0$), the embedded wall predominantly displays a single deformation mode, with the negative (hogging away from the tunnel) maximum bending moment located at the embedded wall's mid-depth position (normalised depth $z/z_t \approx 0.5$), and bending moment increases with embedded wall length. As the embedded wall length increases, the embedded wall's deformation mode transitions from hogging only to a combined sagging (toward the tunnel) and hogging deformed shape, with the maximum bending moment dominated by the sagging component and located close to the tunnel axis ($z/z_t \approx 0.9$-1.0).

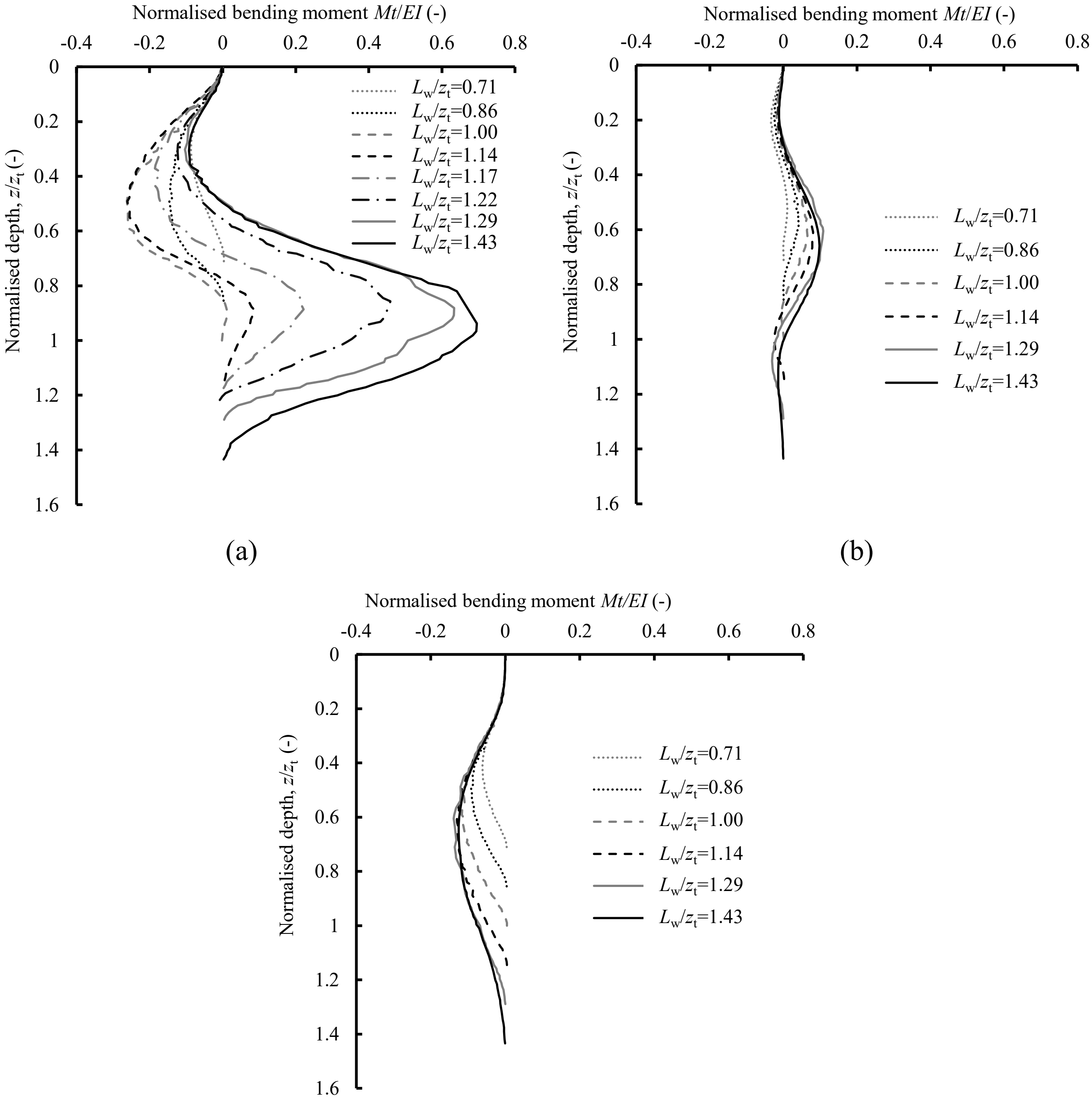

(a) (b)

(c)

Figure 5 FE calculations of the depth-wise profiles of normalised embedded wall bending moments for various embedded wall embedment depths and for embedded wall locations of (a) d_w/D_t=0.61; (b) d_w/D_t=1.11; (c) d_w/D_t=1.61; $V_{l,t}$=3.0%.

For the d_w/D_t =1.11 group, there is a significant decrease in the maximum bending moments compared to the d_w/D_t =0.61 results, and the deformation mode of the embedded wall is characterised by both sagging and hogging zones (see Figure 5(b)). For the shorter embedded walls (L_w/z_t = 0.71, 0.86), the bending moments are negligible; for the relatively long embedded walls, the maximum bending moments are located at $z/z_t \approx 0.6$. Lastly, the response of the embedded walls at a horizontal distance of d_w/D_t =1.61 are considered in Figure 5(c). The results indicate that, unlike the deformation modes of the other two scenarios, the embedded walls in Figure 5(c) primarily exhibit a singular deformation mode (sagging away from the tunnel). An increase in the embedded depth of the embedded wall is shown to have minor effects on the bending moment when L_w/z_t >1.0.

To gain further insight into the response of the embedded walls to tunnel excavation, Figure 6 presents, according to normalised embedded wall depth (L_w/z_t), the maximum value of the normalised bending moment (Figure 6(a)) and the corresponding normalised depth-wise location of this bending moment (z/L_w; Figure 6(b)). From Figure 6(a), the influence of the embedded wall depth on the maximum bending moment is highly dependent on its horizontal proximity to the tunnel: a very close embedded wall shows a variable response with an initial reduction and then a substantial increase in bending moment as the embedded wall is embedded into soil less affected by tunnelling. For the cases of larger tunnel-wall offsets (d_w/D_t =1.11 and 1.61), there is a gradual increase in the maximum bending moment with embedded wall length. Consequently, the embedded wall strength is most critical when placed close to the tunnel.

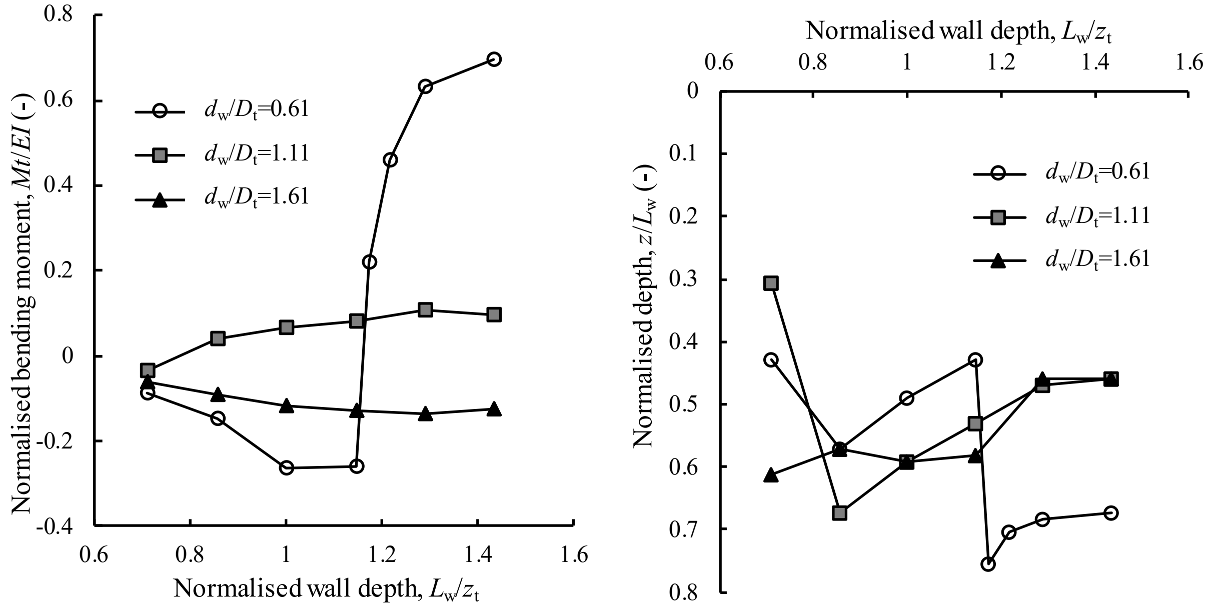

Figure 6 FE calculations of the influence of embedded wall location on the variation of (a) the maximum normalised embedded wall bending moments and (b) their corresponding depth-wise location with normalised embedded wall depth; $V_{l,t}$=3.0%.

Figure 6(b) shows that the normalised depth of the maximum bending moments tend to fluctuate around the middle of the embedded wall ($z/L_w \approx 0.5$), indicating that the central part of the embedded wall tends to be the most vulnerable section. However, for embedded walls positioned at d_w/D_t =0.61, a longer embedded wall ($L_w/z_t > 1.2$) tends to have a deeper ($z/L_w \approx 0.7$) normalised depth of the maximum bending moment, which also corresponds to the highest magnitude of bending moment from Figure 6(a). This location ($z/L_w \approx 0.7$), approximately at the tunnel axis depth, should also be considered in the design stage for a close embedded wall.

3.2 Surface soil displacements

To examine the influence of the embedded wall on tunnelling-induced surface displacements, Figures 7 and 8 display the normalised settlements (U_z/D_t) and horizontal displacements (U_x/D_t) at the soil surface with and without the presence of an embedded wall. Figure 7 demonstrates that the presence of a embedded wall significantly modifies the surface settlement profile, with the alteration being more pronounced for embedded walls situated closer to the tunnel. For the d_w/D_t =0.61 group, Figure 7(a) shows that the embedded walls substantially reduce the exterior (i.e. on the far side of the embedded wall) soil settlements but also contribute to larger interior (on the tunnel-side of the embedded wall) maximum settlements relative to the corresponding greenfield values. Generally, the longer the embedded wall, the more effective it is at reducing settlements on the exterior side of the embedded wall. Note that, in this investigation where a displacement control method was adopted for tunnel volume loss, the embedded wall does not influence the ground loss magnitude or pattern around the tunnel (i.e. wall-tunnel interactions are not simulated); the same "input" of ground loss is imposed on each model and, as such, decreases in settlements on one side of the embedded wall are balanced by increases on the other side. For a pressure/stress control tunnel simulation method, the presence of the embedded wall (particularly for the close embedded wall) may alter the magnitude and shape of ground loss around the tunnel, thus affecting soil displacements and embedded wall response; this aspect was not considered in this study and could be the focus of future work.

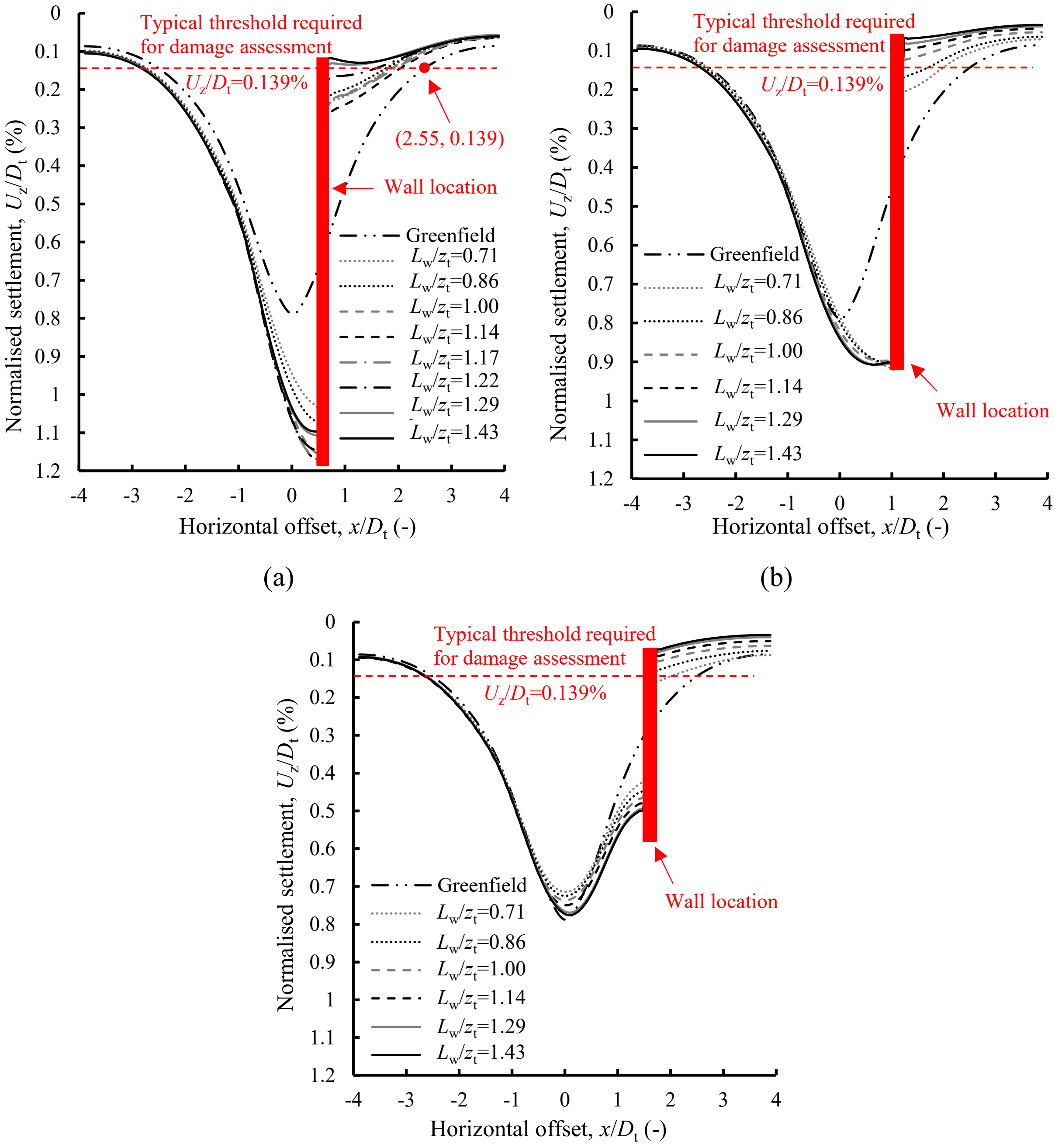

(c)

Figure 7 FE calculations of the influence of embedded wall depth on normalised soil surface settlement for embedded wall locations of: (a) d_w/D_t=0.61; (b) d_w/D_t=1.11; (c) d_w/D_t=1.61; $V_{l,t}$=3.0%.

Similar findings can be deduced for the d_w/D_t =1.11 and 1.61 results in Figures 7(b) and 7(c), where the settlement of the soil on the exterior side of the embedded wall was again notably reduced by the embedded wall. Furthermore, the impact of the embedded wall on the maximum interior soil settlements (compared against the greenfield test) is determined by the horizontal distance of the embedded wall to the tunnel: the farther the embedded wall, the less the impact.

In practice, to assess tunnelling induced building damage, a staged risk assessment procedure proposed by Mair et al. (1996) is often adopted. A typical threshold of settlement in the preliminary assessment stage is 10 mm (corresponding to 0.139% for U_z/D_t), which is also included in Figure 7. First, it is noted that the settlement of the zone at $V_{l,t}$=3.0% within x/D_t=±2.55 exceeds the threshold of 10 mm, indicating the potential necessity of adopting protective measures within this zone. For close embedded walls (d_w/D_t =0.61), it is shown that an embedded wall longer than L_w/z_t = 1.29 can reduce the settlement to this threshold immediately adjacent to the embedded wall, whereas for L_w/z_t = 1.00 and 0.86, settlements reach this threshold at x/D_t= 1.11 and 1.61, respectively. This indicates that the closer the embedded wall is to the tunnel, the longer the embedded wall is required to be to achieve a certain threshold of settlement, consistent with the results reported by Rampello et al. (2019).

The impact of the embedded wall on soil horizontal displacements is examined in Figure 8. For the embedded wall situated at d_w/D_t =0.61, although the embedded wall is effective in minimising exterior soil displacements, there is again a substantial increase in the interior soil displacements compared to greenfield; the longer the embedded wall, the more pronounced the effect, as illustrated in Figure 8(a). Intriguingly, when the embedded wall is located at d_w/D_t =1.11 (Figure 8(b)), there is a decrease in both the interior (left side of the embedded wall) and exterior (right side of the embedded wall) displacements compared against the close embedded wall scenario, and exterior soil displacements are nearly reduced to zero. With a further increase in the horizontal distance to d_w/D_t =1.61, the embedded wall is less effective in minimising exterior horizontal soil displacements, resulting in marginally smaller (but in the same direction) values than the corresponding greenfield case.

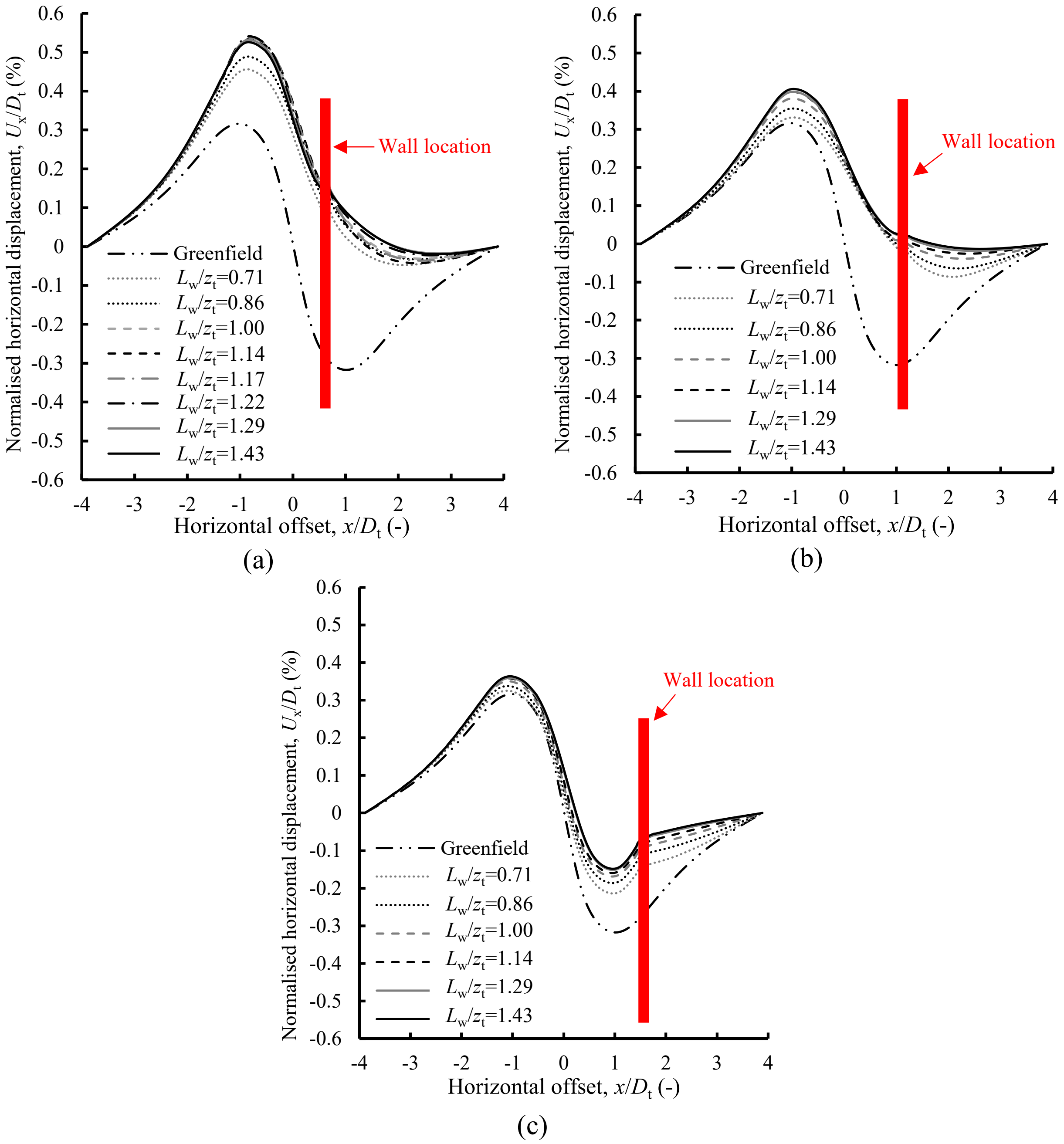

Figure 8 FE calculations of the influence of embedded wall depth on normalised soil surface horizontal displacements for embedded wall locations of: (a) d_w/D_t=0.61; (b) d_w/D_t=1.11; (c) d_w/D_t=1.61; $V_{l,t}$=3.0%.

3.3 Subsurface soil displacement contours

To gain further insights into the settlement mechanisms, this section considers contours of soil settlements (Figure 9(a)) and horizontal displacements (Figure 9(b)) for selected tests; the corresponding greenfield contours were provided in Figure 3. Figure 9(a) shows that the embedded walls significantly affect the spatial distribution of the soil settlements. Interestingly, the close embedded wall (d_w/D_t =0.61) is not as effective as the embedded walls further away (d_w/D_t =1.11 or 1.16) in reducing the exterior settlements, and a larger settlement zone (compared to the greenfield scenario) is formed between the tunnel crown towards the interior side of the embedded wall.

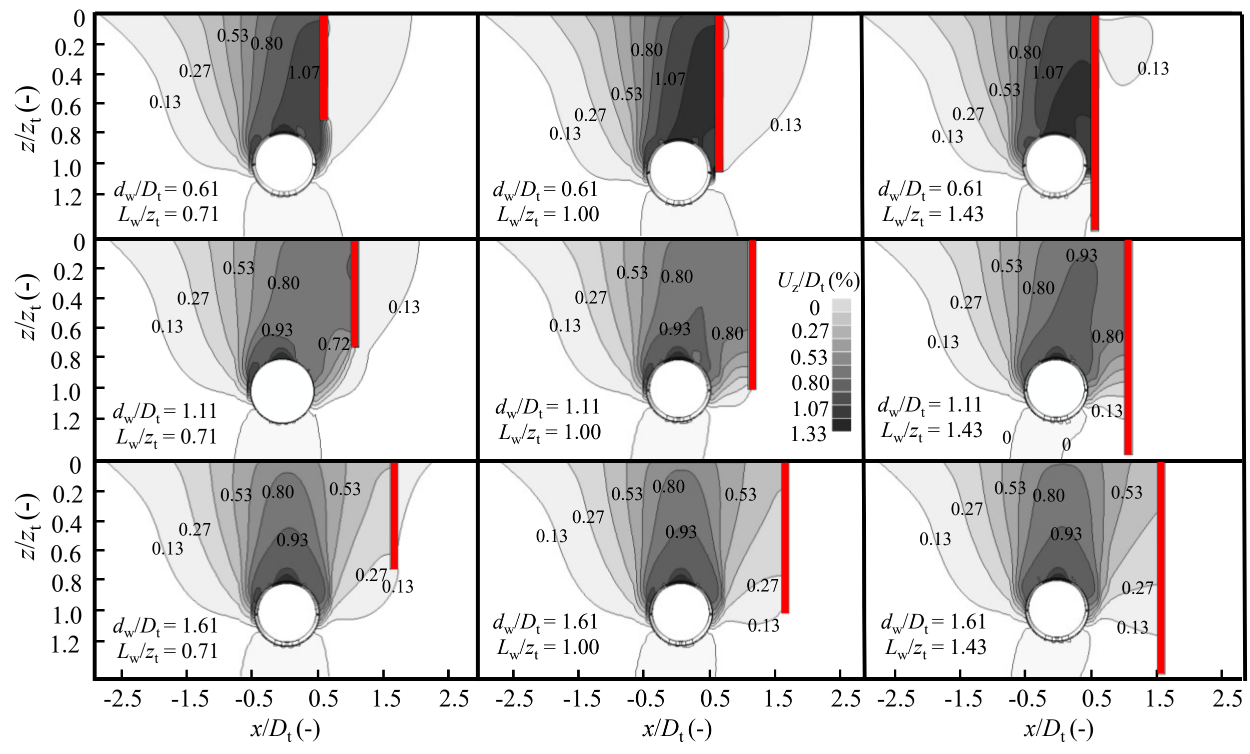

(a)

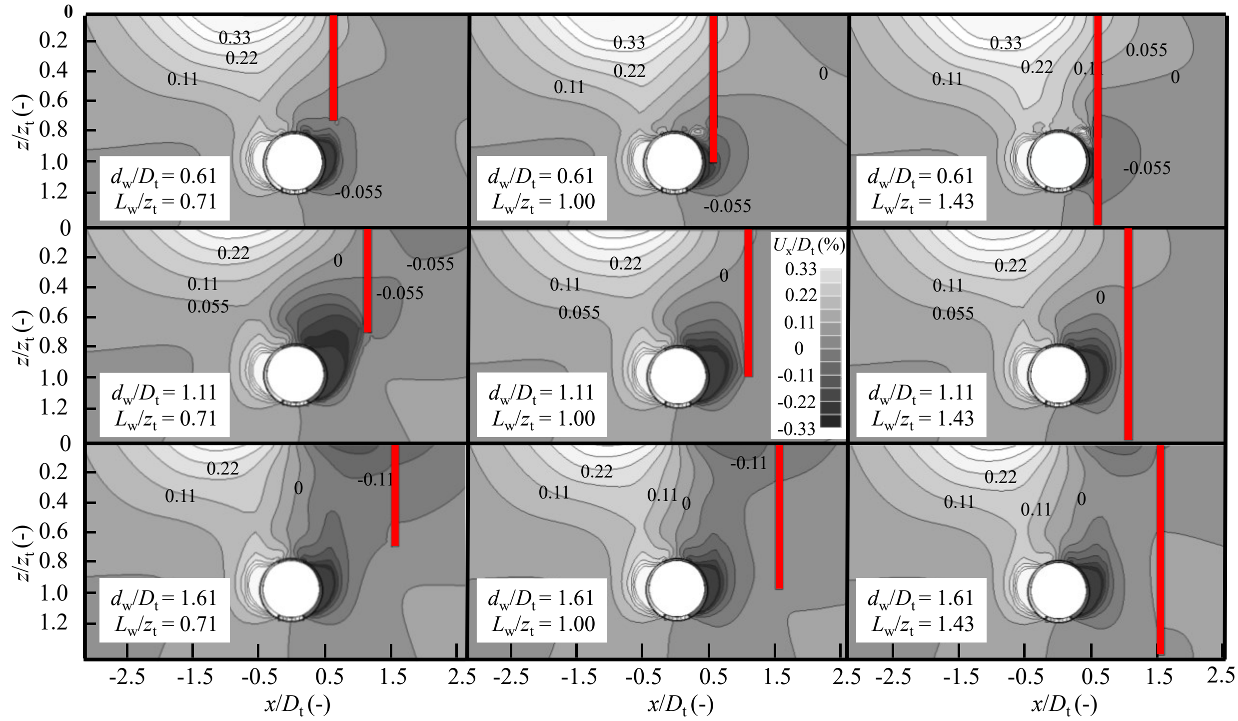

(b)

Figure 9 FE contours of soil displacements: (a) settlements U_z/D_t; (b) horizontal displacements U_x/D_t.

Figure 9(b) shows that, compared against the greenfield scenario in Figure 3, the close embedded wall (d_w/D_t =0.61) altered the direction of the horizontal displacements of the soil adjacent to the exterior side of the embedded wall above a depth of about z/z_t=0.5, causing the soil in this area to move away from the tunnel (contrary to greenfield); this matches with the observed rotation of the embedded wall in Figure 4(a), where the movement of the toe of the embedded wall causes a clockwise rotation of the embedded wall, acting to push the soil near the surface away from the tunnel on the exterior side of the embedded wall. The somewhat counter-intuitive rotational behaviour of the middle embedded wall (d_w/D_t =1.11) presented in Figure 4(b) can be explained here. For the shallower middle embedded walls, a similar mechanism to that of the close embedded wall is observed, with the toe of the embedded wall being pulled towards the tunnel, causing a clockwise rotation of the embedded wall. For the deeper middle embedded walls, where the toe becomes embedded in more stationary ground, Figure 9(b) shows that, nearer the surface, the zone of maximum positive horizontal displacements shifts to the right; this is coincident with a tilting (to the right) of the settlement mechanism above the tunnel in Figure 9(a). These deeper embedded walls prevent ground loss from propagating to the right of the embedded wall and, to compensate for this (for the adopted displacement control method for tunnel ground loss), ground movements are increased on the left side of the embedded wall, causing the observed increase in the size of the area of soil experiencing displacements to the right, and the resulting clockwise rotation/bending of the embedded wall seen in Figure 4(b). For the furthest location from the tunnel (d_w/D_t =1.61), the embedded wall has a minimal effect on the spatial distribution of the soil horizontal displacements where only the horizontal displacements of the near-surface soil on the exterior side of the embedded wall are decreased, and the longer embedded wall tends to have a greater impact.

3.4 Effectiveness of the embedded wall

Bilotta (2008) defined a dimensionless factor η_{bw}^{v} for quantifying the impact of an embedded wall on ground movements due to tunnelling as follows:

$$\eta_{bw}^{v} = \frac{U_{z,ref} - U_{z,bw}}{U_{z,ref}} \tag{1}$$

where $U_{z,bw}$ represents the vertical displacement of the surface soil immediately behind the embedded wall, and $U_{z,ref}$ denotes the reference settlement of the soil at the same location in the greenfield scenario, as shown in Figure 1; an efficiency of 0 indicates no benefit of the embedded wall. Note that the alternative integral efficiency defined by Rampello et al. (2019) may also be used; for the data obtained in this study, the two methods provided consistent results.

It has been suggested that for structures with discontinuous foundations, horizontal soil displacements caused by tunnelling are also a key design concern (Goh and Mair, 2014). Recent centrifuge studies (Xu et al., 2020) have shown that for bare framed structures, the distortion of the frame caused by tunnelling is dominated by shear deformation, which is closely related to the ground slope S. The slope $S = \delta U_z/\delta x$ can be computed as the ratio of the differential settlement at two points on the foundation edges ($\delta U_z = U_{z,A} - U_{z,B}$, see Figure 1) to the horizontal distance ($\delta x=|x_A-x_B|$) separating the two points (with anti-clockwise rotation defined as positive). Consequently, similar dimensional factors are proposed to assess the effect of the embedded wall at reducing the horizontal displacement (η_{bw}^{h}) and the maximum slope (η_{bw}^{s}) of the surface soil behind the embedded wall. These parameters can be calculated using equations analogous to Equation (1). In this study, in calculating η_{bw}^{s}, it was assumed that δx is infinitely small, hence the tangential slope of the settlement curve at the point of interest was used.

Figure 10(a) – (d) presents numerically derived values of η_{bw}^{v} based on soil settlements just behind the embedded walls, η_{bw}^{v} at an offset of x/D_t=1.61 for different embedded wall locations (i.e. based on soil settlements at x/D_t=1.61), η_{bw}^{h}, and η_{bw}^{s}, respectively, and their dependence on the normalised embedded wall depth L_w/z_t, all at $V_{l,t}$=3.0%. Typical thresholds of settlement (10 mm) and slope (1/500) suggested by Mair et al. (1996) for practical use in preliminary damage assessments were used to determine threshold efficiency parameters at different embedded wall locations and are also included in Figure 10(a), (b) and (d). Furthermore, efficiency results from the following cases are also included in Figure 10(a): field testing in sandy ground from Nikiforova and Vnukov (2012), numerical modelling for a scenario with sandy silt and silty sand underlain by sandy gravel and stiff clay from Rampello et al. (2019), and 2D Elastic modelling for undrained soil conditions from Ledesma and Alonso (2017). Due to the differences in soil properties, modelling techniques and volume losses between studies, a direct comparison between the data from the literature and the numerical results obtained here should be avoided; the intention is to allow a more qualitative comparison and to give some context to the outcomes obtained in this study.

For the close embedded walls (d_w/D_t =0.61 in Figure 10(a)), the variation of η_{bw}^{v} with L_w/z_t is highly nonlinear, with η_{bw}^{v} increasing sharply after L_w/z_t >1.17 and stabilising at $\approx$0.8 after L_w/z_t=1.29. In contrast, η_{bw}^{v} increases monotonically with embedded wall length for d_w/D_t=1.11 and 1.61, consistent with Rampello et al. (2019). When considering the thresholds for preliminary risk assessment, only the embedded walls above L_w/z_t=1.29 achieve the necessary efficiency of 0.776 for d_w/D_t =0.61, whereas for d_w/D_t =1.11 the critical embedded wall length to achieve the necessary efficiency of 0.653 is L_w/z_t=1.00, and for d_w/D_t =1.61 the critical embedded wall length to achieve the necessary efficiency of 0.340 is reached at about L_w/z_t=0.9.

Practically, the shallowest embedded wall is desirable to reduce costs. Considering an example where a structure is located near the position of x/D_t =1.61 for the parameters adopted here, where the greenfield settlement exceeds the settlement threshold (see Figure 7(a)), Figure 10(b) demonstrates that the embedded wall at d_w/D_t =1.11 is likely the best option. Whilst the closest embedded wall (d_w/D_t =0.61) meets the settlement threshold criteria even for short embedded walls, a conservative efficiency is not reached until embedded wall length exceeds about L_w/z_t=1.22. The embedded wall at d_w/D_t =1.11 achieves the highest settlement efficiency at the location x/D_t =1.61 for a reasonable embedded wall depth of ~L_w/z_t=1.0.

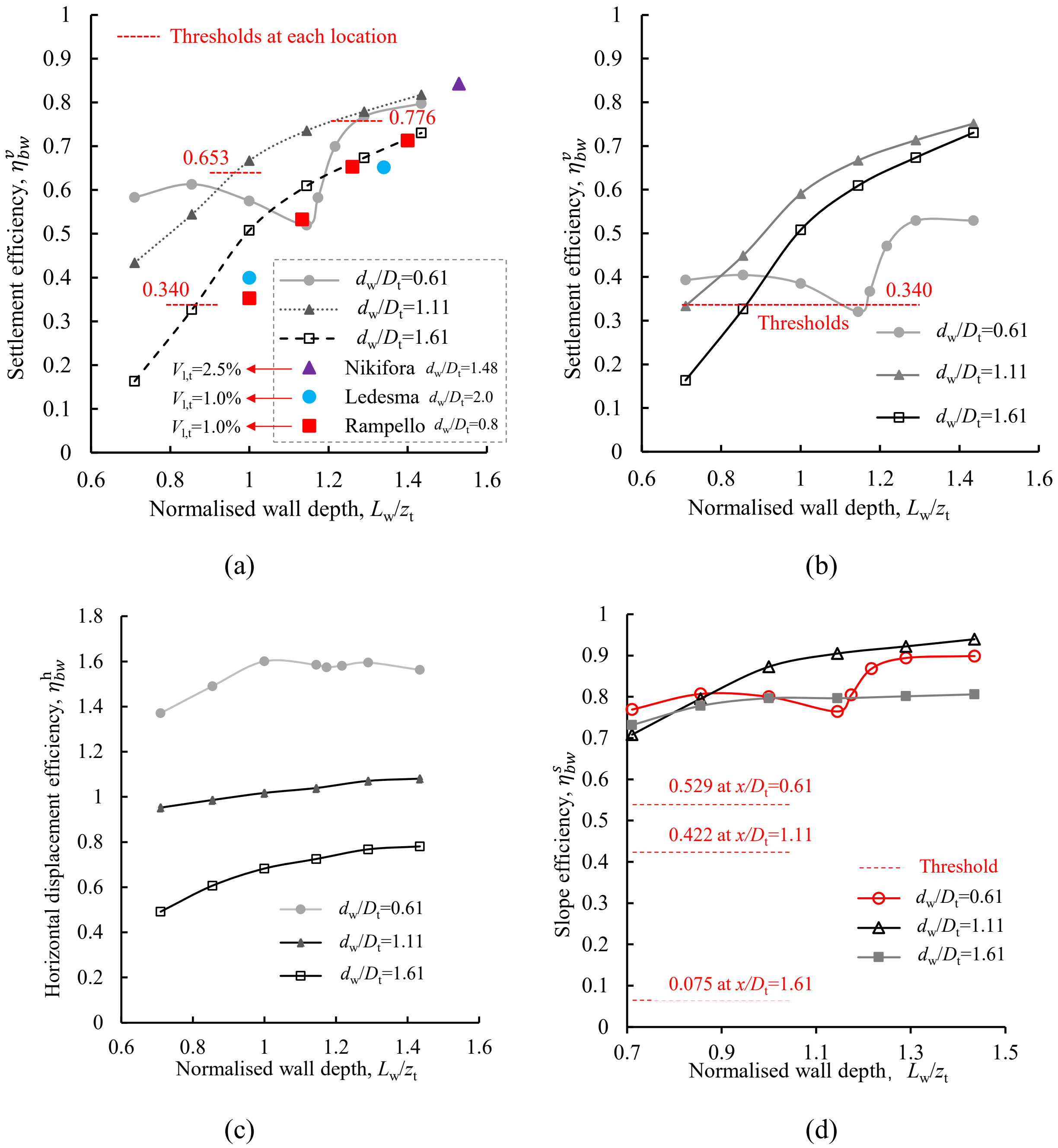

Figure 10 Efficiency parameters and their dependence on embedded wall depth and location: (a) soil settlement η_{bw}^{v} just behind embedded walls (including data from Nikiforova and Vnukov (2012), Rampello et al. (2019) and Ledesma and Alonso (2017)), (b) soil settlement η_{bw}^{v} at

x/D_t=1.61, (c) horizontal displacement of the soil η_{bw}^{h} just behind the embedded walls and (d) surface slope of the soil η_{bw}^{s} just behind the embedded wall; $V_{l,t}$=3.0%.

Figure 10(a) also shows that, despite the embedded wall efficiency values being obtained for different soil properties, embedded wall locations and methodologies, there is good agreement between data points from literature sources, with slightly higher settlement efficiencies for sandy ground obtained in this study and in Nikiforova and Vnukov (2012). The results further confirm the dominant role of embedded wall length L_w/z_t in reducing tunnelling induced ground displacements, consistent with Bilotta (2008), Bilotta and Stallebrass (2009), and Franza et al. (2021).

In contrast to settlements, Figure 10(c) shows that η_{bw}^{h} is more sensitive to the horizontal location of the embedded wall. Interestingly, the presence of the close embedded wall alters the direction of the horizontal displacement of the soil (η_{bw}^{h} is greater than 1), whereas the embedded walls at d_w/D_t =1.11 achieve an efficiency of $\eta_{bw}^{h} \approx 1$ for all embedded wall lengths. Note that an efficiency of 1.4 is equivalent in terms of displacement magnitude to 0.6, but in the opposite direction, hence the embedded walls at d_w/D_t =0.61 and 1.61 perform about the same in terms of horizontal displacements.

Finally, Figure 10(d) shows that the embedded walls are effective in reducing the slope of the soil surface, with efficiency value of η_{bw}^{s} for all embedded walls greater than 0.7, which is sufficiently safe for all locations (Mair et al., 1996).

4 Discussion

The present numerical results indicate that both the length and horizontal distance of the embedded wall from the tunnel can significantly influence ground displacements caused by tunnelling. Their effects on ground movements are highly nonlinear, as demonstrated in Figure 10. This poses significant challenges for engineers when attempting to use embedded walls to protect structures from tunnelling-induced damage.

For embedded walls situated very close to the tunnel (e.g. d_w/D_t =0.61), Figure 11(a) highlights the nonlinear relationships between embedded wall settlement, tunnel volume loss and embedded wall length, with a maximum settlement of 0.86%D_t (and associated drop in η_{bw}^{v} in Figure 10(a)) when L_w/z_t =1.14. These results indicate that when the toe of the embedded wall is located very close to the tunnel, the settlement of the embedded wall becomes significant (larger than the corresponding greenfield surface displacement), and, in turn, the embedded wall's ability to reduce tunnelling induced soil displacements diminishes, as also pointed out by Ledesma and Alonso (2017). Conversely, for the embedded walls positioned at d_w/D_t =1.11 and 1.61 (Figures 11(b)-(c)), their settlement generally decreases monotonically with their length, resulting in a continuous increase of the efficiency parameter η_{bw}^{v} (see Figures 10 (a)), consistent with Rampello et al. (2019). Moreover, for η_{bw}^{h} and η_{bw}^{s}, the intermediate embedded wall location (d_w/D_t =1.11) is optimal, and its bending moment and horizontal displacement are considerably smaller than the embedded wall situated very close to the tunnel (see Figures 4-6).

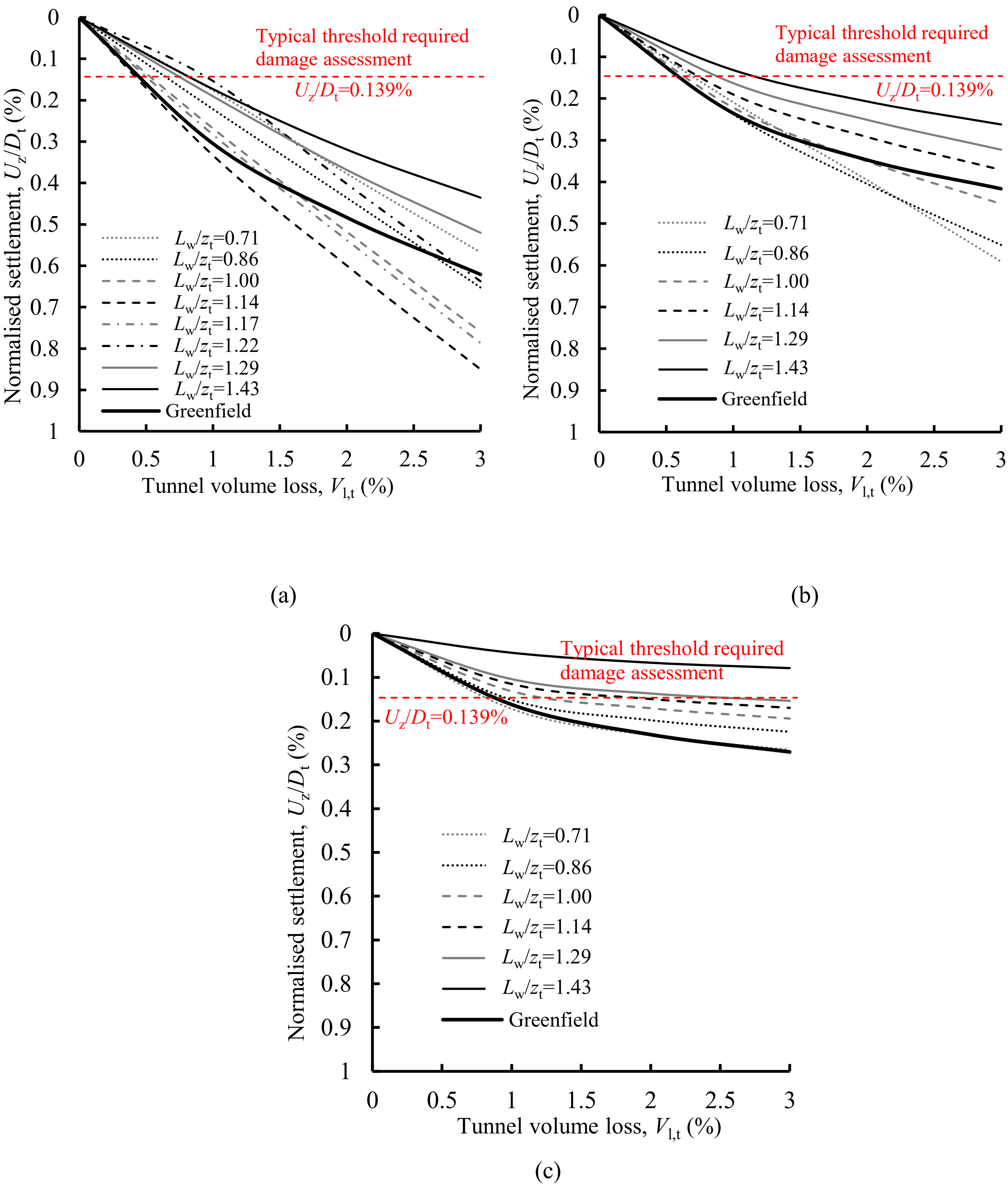

Figure 11 FE calculations of the influence of embedded wall depth on the variation of normalised embedded wall settlements with tunnel volume loss for embedded wall locations of: (a) d_w/D_t=0.61; (b) d_w/D_t=1.11; (c) d_w/D_t=1.61

The numerical outputs were used to develop a preliminary design chart for determining the optimal horizontal location and depth of an embedded wall to reduce tunnelling-induced ground displacements, as shown in Figure 12. The chart is based on a relatively high tunnel volume loss $V_{l,t}$=3.0%; at lower values of tunnel volume loss, efficiency values tend to be higher (see η^{v}_{bw} values at $V_{l,t}$=1.0% in Figure S3), however the outcomes are consistent with the design chart in Figure 12.

For close embedded walls, caution should be exercised when selecting the depth of the embedded wall, as an embedded wall with its toe close to the tunnel tends to settle significantly, thereby reducing the embedded wall's efficiency. For this case, an embedded wall length of L_w/z_t >1.3 is recommended, as it can reduce ground settlement with an efficiency value $\eta^{v}_{bw} \approx 0.8$ (below the preliminary assessment threshold from Mair et al. (1996)).

Embedded walls positioned in the region 0.9< d_w/D_t <1.2 are likely the optimal solution, as they can reduce soil settlements and surface slope with higher efficiency than embedded walls closer and farther from the tunnel, whilst also significantly restricting horizontal soil displacements. To support this conclusion, efficiency values are plotted against normalised wall distance from the tunnel in Figure S4 of the Supplemental Materials, including results from additional models not discussed above (L_w/z_t=1.14≈1.1; d_w/D_t =0.86, 1.20, 1.30 and 1.40); the data demonstrate that, in the region 0.9< d_w/D_t <1.2, an embedded wall with L_w/z_t >1.1 can reduce soil settlement with an efficiency η^{v}_{bw} >0.7 (sufficient for a preliminary damage assessment). Finally, embedded wall lengths of L_w/z_t >=1.0 at d_w/D_t >1.5 are likely to generate satisfactory efficiencies to meet preliminary damage assessment criteria, however for this embedded wall depth, an embedded wall placed at an intermediate location will likely provide greater efficiencies, and will more effectively reduce horizontal displacements.

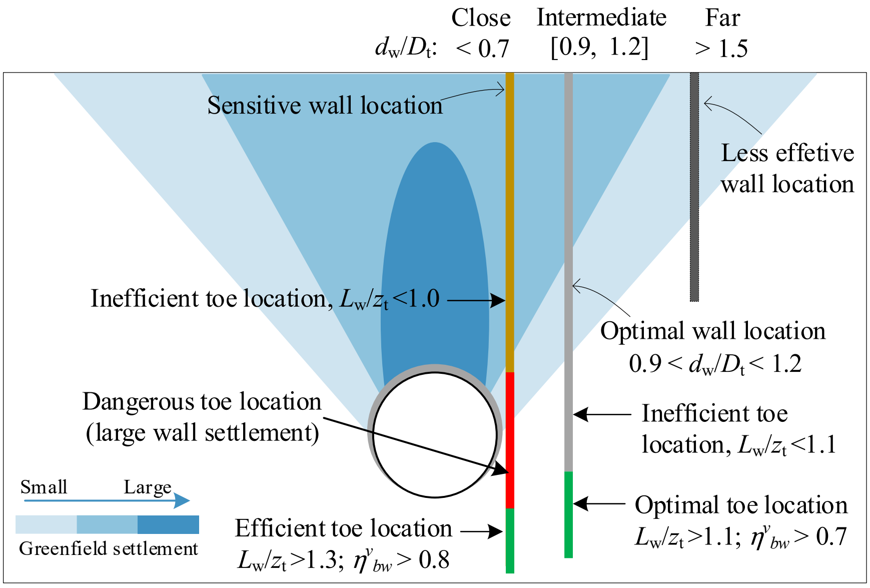

Figure 12 Design chart to inform an optimal choice of the depth and horizontal distance of an embedded wall (based on relatively high tunnel volume loss $V_{l,t}$=3.0%; effects of wall construction are not included)

Limitations arising from some of the assumptions adopted for the numerical modelling should be noted. First, the embedded walls were assumed to be “wished-in-place” and thus not causing any ground movements during construction of the embedded walls. A recent numerical study by Rampello et al. (2019) suggested that the wall installation (excluding construction) causes minimal ground displacements. In reality, however, the displacements caused by embedded wall construction may not be negligible, and in some cases, may account for the majority of the final surface settlement, as documented by Gens et al. (2005). Furthermore, as a consequence of the wished-in-place walls adopted here, the wall installation effects on the tunnel-wall interactions were not captured within the numerical modelling outcomes, however these are believed to play a secondary role in the overall interaction problem (future work may consider this aspect). Second, this paper assumed a perfectly rough soil-structure interface (a friction coefficient of tan (φ'_c) = 0.62) for the soil-embedded wall interface. This provides a conservative outcome in Figure 12 as previous studies (centrifuge tests by Bilotta (2008) and numerical modelling by Rampello et al., 2019) have shown that a smoother soil-wall interface results in higher local efficiencies due to lower downwards shear stresses applied by the wall to the soil. Finally, the tunnelling process was simulated numerically using a displacement control method; the adoption of a pressure control method may result in slightly different local efficiency values and design chart; again this could be an area of further study.

5 Conclusions

This paper presented a comprehensive numerical investigation into the effects of embedded walls on tunnelling-induced ground displacements, providing valuable insights into the optimal design of embedded walls for urban tunnelling projects. The study has shown that the efficiency of embedded walls in reducing tunnelling-induced ground displacements is influenced by both embedded wall length and horizontal distance from the tunnel, with the relationship between these factors being nonlinear and highly inter-dependent.

The findings reveal that embedded walls located at a horizontal distance of $0.9 < d_w/D_t < 1.2$ from the tunnel are likely to offer the best balance between settlement reduction, horizontal displacement restriction, and structural efficiency. Additionally, an embedded wall length of $L_w/z_t > 1.1$ is suggested as the optimal depth at this location, resulting in an efficiency >0.7 which, based on the current study, was sufficient for mitigating the potential structural damage due to tunnelling.

However, for embedded walls situated extremely close to the tunnel (d_w/D_t < 0.7), the depth selection requires careful consideration to avoid excessive settlement and decreased efficiency, and an embedded wall length of L_w/z_t > 1.3 is suggested.

A design chart was presented to serve as a tool for engineers to determine preliminary embedded wall (horizontal) locations and depths in the context of tunnelling projects. Whilst the findings contribute to a better understanding of embedded wall performance, it is important to acknowledge that site-specific conditions and soil properties may affect the results. Furthermore, limitations arising from the simplification of the numerical modelling should be also noted. Therefore, further investigation and validation through physical experiments or additional numerical analyses are recommended to enhance the general applicability of the design chart.

Acknowledgments

This research has received funding from the National Natural Science Foundation of China (Grant No. 52108364, 52278398) and the Royal Society (Grant No. 211179).

References

Bilotta, E., 2008. Use of diaphragm walls to mitigate ground movements induced by tunnelling. Geotechnique 58, 143-155.

Bilotta, E., Russo, G., 2011. Use of a line of piles to prevent damages induced by tunnel excavation. Journal of geotechnical and geoenvironmental engineering 137, 254-262.

Bilotta, E., Stallebrass, S.E., 2009. Prediction of stresses and strains around model tunnels with adjacent embedded walls in overconsolidated clay. Computers and Geotechnics 36, 1049-1057.

Boldini, D., Losacco, N., Bertolin, S. and Amorosi, A., 2018. Finite element modelling of tunnelling-induced displacements on framed structures. Tunnelling and underground space technology, 80, 222-231.

Boonsiri, I., Takemura, J., 2015. Observation of Ground Movement with Existing Pile Groups Due to Tunneling in Sand Using Centrifuge Modelling. Geotechnical and Geological Engineering, 33, 621–640.

Burland, J.B. 2001. Assessment methods used in design. In J.B. Burland, J.R. Standing & F.M. Jardine (eds.) Building response to tunnelling. Case studies from construction of the Jubilee Line extension, London 1: 23–43.

Di Mariano, A., Gesto, J.M., Gens, A. and Schwarz, H., 2007, October. Ground deformation and mitigating measures associated with the excavation of a new Metro line. In Proc. XIV European Conference on Soil Mechanics and Geotechnical Engineering, ECSMGE (pp. 1901-1906).

Franza, A., Losacco, N., Ledesma, A., Viggiani, G.M.B. and Jimenez, R., 2021. Protecting surface and buried structures from tunnelling using pile walls: a prediction model. Canadian Geotechnical Journal, 58(10), pp.1590-1602.

Fu, J., Yu, Z., Wang, S. and Yang, J., 2018. Numerical analysis of framed building response to tunnelling induced ground movements. Engineering Structures, 158, 43-66.

Gens, A., Di Mariano, A., Gesto, J.M. and Schwarz, H., 2005. Ground movement control in the construction of a new metro line in Barcelona. Geotechnical aspects of underground construction in soft ground, pp.389-395.

Goh, K.H. and Mair, R.J., 2014. Response of framed buildings to excavation-induced movements. Soils and Foundations, 54(3), pp.250-268.

Harris, D.I. 2001. Protective measures. In J. B. Burland, J.R. Standing & F.M. Jardine (eds.) Building response to tunnelling. Case studies from construction of the Jubilee Line extension, London 1: 135–168.

Herle, I., Gudehus, G., 1999. Determination of parameters of a hypoplastic constitutive model from properties of grain assemblies. Mech. Cohesive-Frict. Mater. 4 (5), 461–486.

Hibbitt, K., 2002. ABAQUS/Explicit User's Manual: Version 6.3. Hibbit, Karlsonn & Sorensen.

Khalajzadeh, A.K., Choobbasti, A.J. and Kutenaei, S.S., 2023. Dynamic behaviour of a circular tunnel in the sand: A numerical verification of a centrifuge program. Tunnelling and Underground Space Technology, 138, p.105152.

Lanzano, G., Visone, C., Bilotta, E. and Santucci de Magistris, F., 2016. Experimental assessment of the stress–strain behaviour of Leighton Buzzard sand for the calibration of a constitutive model. Geotechnical and Geological Engineering, 34, pp.991-1012.

Ledesma, A., Alonso, E.E., 2017. Protecting sensitive constructions from tunnelling: the case of world heritage buildings in Barcelona. Geotechnique 67, 914-925.

Losacco, N., Viggiani, G.M., 2019. Mechanised tunnel excavation through an instrumented site in Rome: Class a predictions and monitoring data, in: National Conference of the Researchers of Geotechnical Engineering, Springer. pp. 245-254.

Mair, R.J., Taylor, R.N. and Burland, J.B., 1996. Prediction of ground movements and assessment of risk of building damage due to bored tunnelling. In Geotechnical aspects of underground construction in soft ground (pp. 713-718).

Nikiforova, N., and Vnukov, D. 2012. Geotechnical cut-off diaphragms for built-up area protection in urban underground development. In Geotechnical Aspects of Underground Construction in Soft Ground: Proceedings of the 7th International Symposium on Geotechnical Aspects of Underground Construction in Soft Ground, Roma, Italy, 17–19 May 2011. Edited by G. Viggiani. CRC Press, Leiden, the Netherlands. pp. 927–932.

Rampello, S., Fantera, L. and Masini, L., 2019. Efficiency of embedded barriers to mitigate tunnelling effects. Tunnelling and Underground Space Technology, 89, pp.109-124.

Song, G., Marshall, A.M., 2021. Centrifuge study on the use of protective walls to reduce tunnelling-induced damage of buildings. Tunnelling and Underground Space Technology, 115, p.104064.

Song, G., Marshall, A.M., 2020a. Centrifuge modelling of tunnelling induced ground displacements: pressure and displacement control tunnels. Tunnelling and Underground Space Technology, 103, p.103461.

Song, G., Marshall, A.M., 2020b. A centrifuge study on the influence of tunnel excavation on piles in sand. Journal of Geotechnical and Geoenvironmental Engineering. 146 (12), 04020129.

Song, G., Xu, J., & Marshall, A. M. (2023). Numerical study on the effect of protective wall depth in reducing structure deformations caused by tunnelling. Computers and Geotechnics, 158, Article 105374.

von Wolffersdorff, P.-A., 1996. A hypoplastic relation for granular materials with a predefined limit state surface. Mech. Cohesive-Frict. Mater. 1 (3), 251–271.

Wang, C., Ding, X., Cao, G., Jiang, C., Fang, H. and Wang, C., 2022. Numerical investigation of the effect of particle gradation on the lateral response of pile in coral sand. Computers and Geotechnics, 152, p.105012.

Xu, J., Franza, A. and Marshall, A.M., 2020. Response of framed buildings on raft foundations to tunneling. Journal of Geotechnical and Geoenvironmental Engineering, 146(11), p.04020120.

Youd, T.L., 1973. Factors controlling maximum and minimum densities of sands. In: Evaluation of relative density and its role in geotechnical projects involving cohesionless soils. ASTM International.

Zhao Y. In situ soil testing for foundation performance prediction. PhD thesis, University of Cambridge, 2008.

Supplemental Materials

To obtain the parameter values in the hypoplastic model, Song and Marshall (2020a) describes a detailed approach. The critical state friction angle φ'_c was obtained based on five heap tests. Herle and Gudehus (1999) suggested that the initial void ratio in a proportional compression test (i.e. an oedometer test) with very loose sand can be considered as an appropriate estimate of e_{c0}. Herle and Gudehus (1999) defined granular hardness h_s as:

$$h_s = 3p'\left(\frac{ne_p}{C_c}\right) \tag{S1}$$

where $C_c = \Delta e/\Delta \ln p'$ is the tangent compression index.

Using data from an oedometer test and considering two values of C_c at different magnitudes of mean effective stress p' (i.e. two points on an $e - \ln(p')$ curve; indicated below by subscripts 1 and 2), Equation (S1) can be used to obtain an expression for n:

$$n = \frac{\ln(e_1 C_{c2}/e_2 C_{c1})}{\ln\left(p'_2/p'_1\right)} \tag{S2}$$

Using the above approach on data obtained from an oedometer test on Fraction E sand (see Figure S1), values of e_{c0}=1.16, h_s=1969MPa and n=0.447 were obtained.

The value of minimum void ratio at zero pressure e_{d0} can be determined using (Herle and Gudehus, 1999):

$$e_{d0} = e_d \exp\left[\left(3p'/h_s\right)^n\right] \tag{S3}$$

where the value of e_d mainly depends on the coefficient of uniformity C_u and grain shape. Youd (1973) measured the value of e_d using a simple shear test under a vertical pressure of 96 kPa, corresponding to $p' \approx 55$ kPa (based on assumption of K_0=0.4), and proposed a diagram relating e_d to grain angularity and C_u. Based on the diagram of Youd (1973), a value of e_d=0.615 was obtained.

By substituting this value into Equation (S3) (along with previously determined parameter values), a value of e_{d0}=0.624 was obtained. As suggested by Herle and Gudehus (1999), the value of maximum void ratio at zero pressure e_{i0} can be approximated as $e_{i0} \approx e_{c0} \times 1.2$, therefore, the critical void ratio at zero pressure e_{i0} was determined as 1.392.

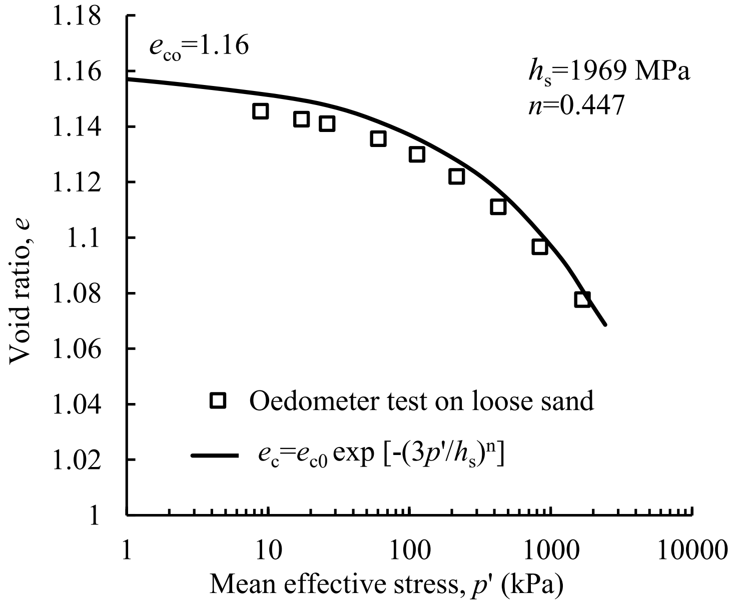

Figure S1 Oedometer test data and numerical results for Leighton Buzzard Fraction E sand (modified from Song and Marshall, 2020a)

Two drained triaxial compression tests were conducted at an effective confining pressure of 200 kPa using the same sand, with the same relative density of I_d = 90%. To calibrate the parameters α and β, a single 3D brick element (C3D8) numerical analysis was conducted in ABAQUS to replicate the triaxial tests. Figure S2 shows that numerical simulation results using α=0.065 and β=0.3 compare well against both the triaxial volumetric data and the non-linear stress–strain response of the soil.

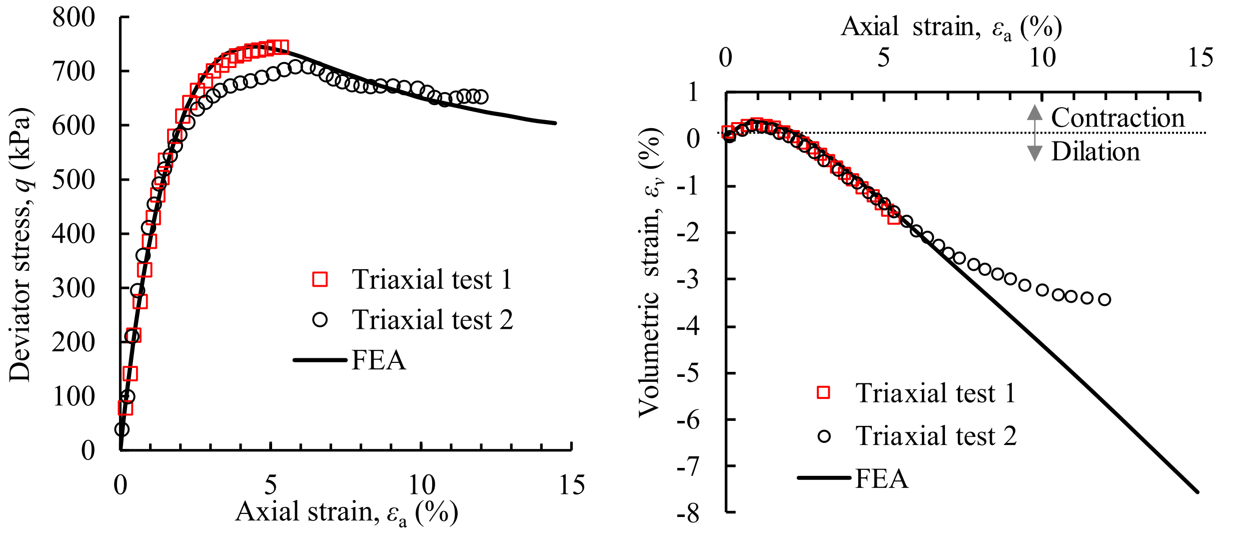

(a) (b)

Figure S2 Drained triaxial test data for Leighton Buzzard Fraction E sand and numerical (FEA) results using hypoplastic model (effective confining stress = 200kPa): (a) Deviator stress; (b) Volumetric strain; modified from Song and Marshall (2020a)

To compare the efficiency η_{bw}^{v} values at a low tunnel volume loss with those obtained at a high tunnel volume loss, the settlement efficiency η_{bw}^{v} values at $V_{l,t}$=1.0% for all embedded walls are presented in Figure S3. Results show that η_{bw}^{v} values at low $V_{l,t}$=1.0% tend to be higher than those at $V_{l,t}$=3.0%.

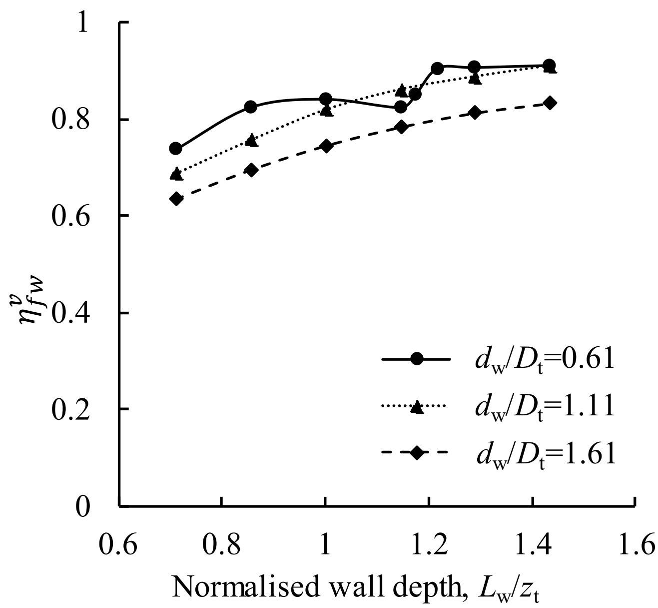

Figure S3 Efficiency parameter η^{v}_{bw} with embedded wall depth and location at $V_{l,t}$=1.0%.

To support the design chart presented in Figure 12, results from an additional four models at d_w/D_t =0.86, 1.20, 1.30 and 1.40 are considered; the length of all models is L_w/z_t=1.14≈1.1. The resulting efficiency values are plotted against normalised wall distance from the tunnel in Figure S4. Results shows that, in the region 0.9< d_w/D_t <1.2, an embedded wall with L_w/z_t >1.1 can reduce soil settlement with an efficiency η^{v}_{bw} >0.7.

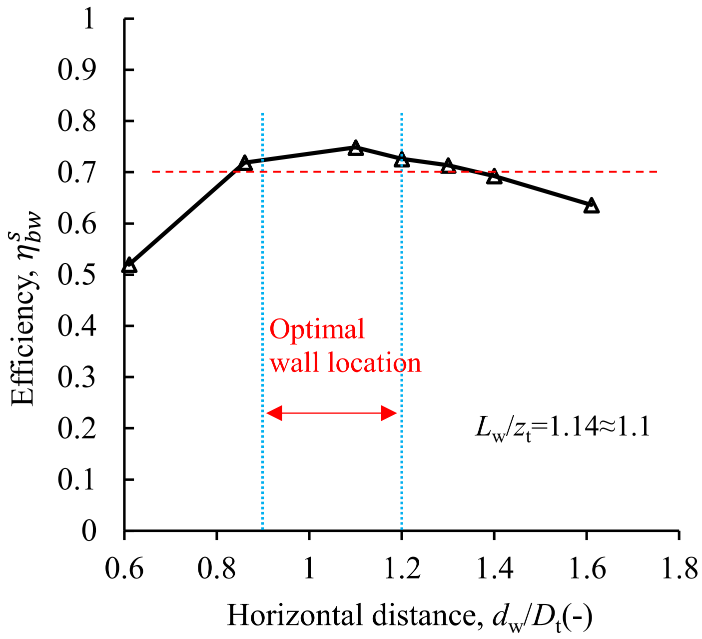

Figure S4 Efficiency parameter η_{bw}^{v} with horizontal distance d_w/D_t to the tunnel for walls with L_w/z_t=1.14≈1.1.